2. Recent research activities

2.1. Molecular rectification using a porphyrin chain

The main challenge in the molecular electronics is to establish that single molecules or a finite number of self-assembled molecules can perform all the basic functions of conventional electronic components such as wires, diodes and transistors. The realization of a molecular device with a unimolecular rectifying function is one of the most important and fundamental requirements in nanotechnology. Aromatic molecules have π-conjugation systems through which electrons can flow easily. By substituting different functional groups on an aromatic system it is possible to increase or decrease the π-electron density and thereby creating acceptor (p-type) and donor (n-type) molecular subunits. Therefore, a rectifier could be built by combining these two molecular subunits between two electrodes, in which electrons can flow from cathode to the acceptor or from donor to the anode [14–16]. In this strategy to realize a rectifying function, HOMO and LUMO have to localize on a donor and an acceptor, respectively. Porphyrin possesses good electron-donating properties due to its large easily ionized π-electron system and a long molecular wire of fully conjugated porphyrin polymer has been reported by Tsuda and Osuka [32]. In this study, we propose that a rectifier diode can be created by combining two metal porphyrin molecules with different transition metal atoms. This porphyrin polymer would be a potential candidate for a several applications: molecular wires in molecular electronics; materials for nonlinear optic devices; near-infrared (near-IR) dyes; spintronics devices, etc. In order to describe the electron transport through this polymer, we have analyzed the spatial distribution of the frontier orbitals (HOMO and LUMO), suggesting a strategy by which the rectifying properties of the porphyrin polymer can be understood.

Many configurations of porphyrin polymers have been already synthesized [32]. Fig. 1 indicates the different structures of porphyrin polymers investigated in this study. Fig. 1(a)–(c) are fully-, partially-, and non-conjugated free base porphyrin chains, respectively. These polymers have been chosen to permit the evaluation of the effect of the molecular structure on the localization of their frontier orbitals.

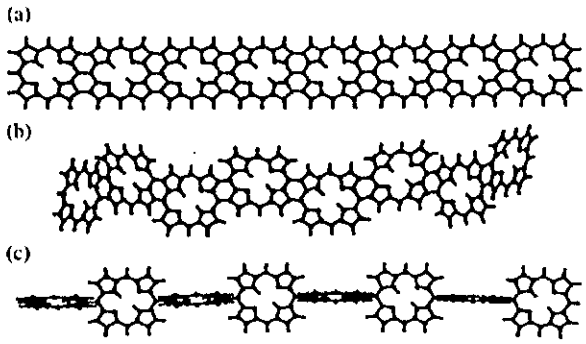

Fig. 1. Stable structure of (a) fully conjugated, (b) partially conjugated and (c) non-conjugated free base porphyrin chain at the HF/3-21G level.

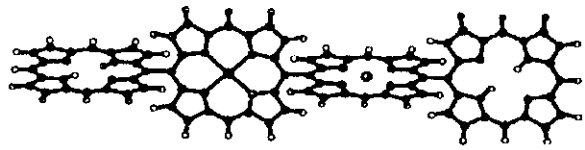

Fig. 2. Four porphyrin monomers, arranged as a metal–metal junction in porphyrin chain.

In this study, we investigate four porphyrin monomers, forming a metal-metal junction in a porphyrin polymer, inserting two transition metal porphyrins in the center of the polymer (see Fig. 2). Typical results of the orbital spatial distribution in a porphyrin polymer obtained by HF/6-311G are shown in Figs. 3–5 and Table 1. In Table 1, 'No' means that these molecules did not show the rectifying function. It is assumed that the unoccupied orbitals provide channels for electron conduction through the molecules. The difference in the energy of the lowest unoccupied levels between a donor and an acceptor was used to estimate a criterion (potential drop) of a rectifying function. The potential drop in a vacuum can be explained as the difference in the LUMO energies between the donor and acceptor molecules when they are widely separated ($\Delta E_{\mathrm{LUMO}}(\infty) = E_{\mathrm{LUMO}}(\mathrm{donor}) - E_{\mathrm{LUMO}}(\mathrm{acceptor})$) [14]. It is clearly seen from Fig. 3 that a full planar structure (fully conjugated) does not exhibit the rectification properties (except for the case of Cr–Cu in which the empty porphyrin plays donor function).

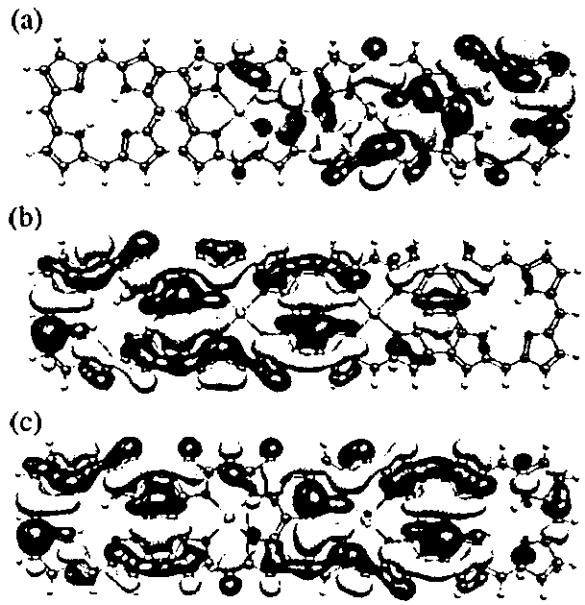

Fig. 3. Orbital spatial orientation of the frontier orbital for the Zn–Fe pair in fully conjugated porphyrin chain. (a) HOMO, (b) LUMO, and (c) LUMO + 1.

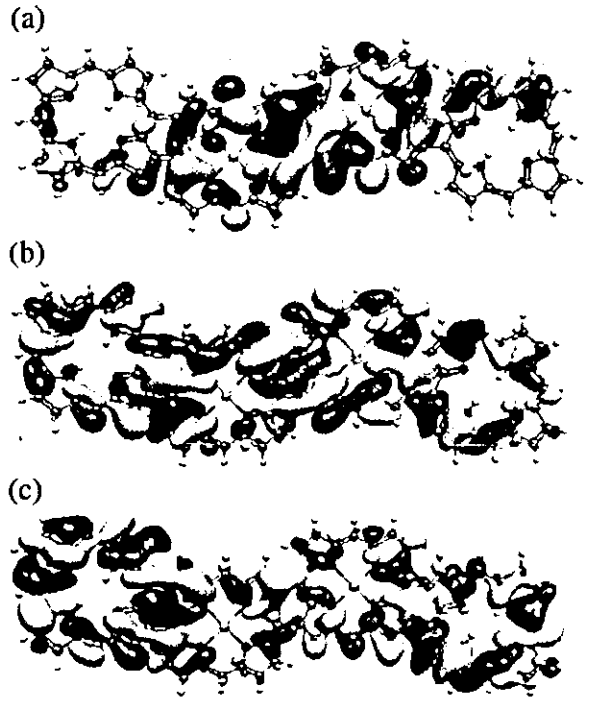

Fig. 4. Orbital spatial orientation of the frontier orbital for the Zn–Ni pair in partially conjugated porphyrin chain. (a) HOMO, (b) LUMO, and (c) LUMO + 1.

Moreover, similar results are obtained for a partially conjugated chain. Fig. 4 clearly indicates that HOMO and LUMO are delocalized on a whole polymer. A rectifier is reported in the case of a D(donor)–π-A(acceptor) structure [33,34], even though, this porphyrin polymer does not

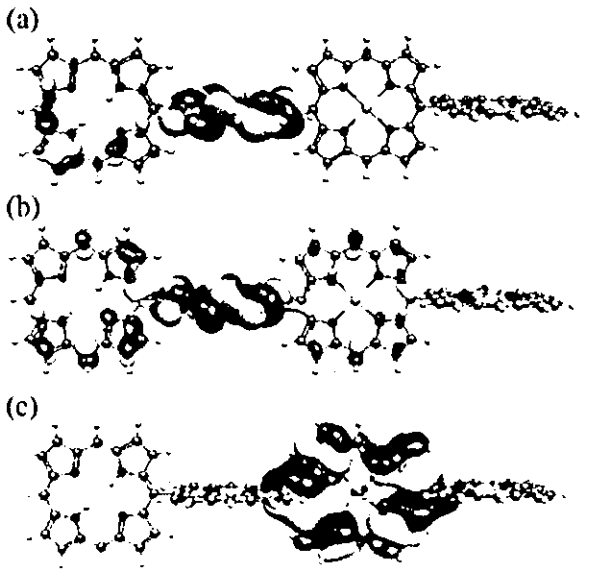

Fig. 5. Orbital spatial orientation of the frontier orbital for the Cr–Cu pair in non-conjugated porphyrin chain. (a) SOMO, (b) LUMO, and (c) LUMO + 5.

Table 1
Calculation summary

Structure	ΔE_{LUMO} (eV)	$\Delta E_{HOMO-LUMO}$ (eV)
Fully conjugated (Cr–Cu)	1.59	5.37
Fully conjugated (Zn–Zn)	No	4.30
Fully conjugated (Zn–Fe)	No	4.32
Fully conjugated (Zn–Ni)	No	4.35
Partially conjugated (Zn–Zn)	No	5.13
Partially conjugated (Zn–Ni)	No	5.13
Non conjugated (Cr–Cu)	0.54	7.36
Non conjugated (Zn–Zn)	No	6.18
Non conjugated (Zn–Fe)	0.11	6.16
Non conjugated (Zn–Ni)	0.02	6.18

ΔE_{LUMO} indicates an energy difference between LUMO + K localized on a donor and LUMO on an acceptor. $\Delta E_{HOMO-LUMO}$ indicates the HOMO–LUMO gap. ΔE_{LUMO} and $\Delta E_{HOMO-LUMO}$ are obtained using HF/6-311G.

exhibit the localized frontier orbital. However, a non-conjugated chain displays rectifying features (Cr–Cu and Zn–Fe). HOMO and LUMO + 5 for Cr–Cu in the non-conjugated polymer form the localized donor side (Cu porphyrin) and LUMO forms the localized acceptor side (Cr porphyrin). Consequently, these results together with previous reports [14–16] indicate that the geometry of spacer plays an important role in localizing the frontier orbitals.

2.2. *Molecular photovoltaic cell*

Conjugated polymers emerged in the mid-80s to early-90s and were developed for a wide range of opto-electronic applications such as organic transistors, light emitting diodes, and solar cells. The current general trend in research and development of photovoltaic elements is aimed at producing lower cost devices. Solar cells based on conjugated polymers alone have been disappointing because of their low quantum efficiencies. However, an encouraging breakthrough in the development of highly efficient materials has been achieved by mixing electron-donor type polymers with suitable electron acceptors [35,36]. Accordingly, photovoltaic elements based on conjugated polymer, have attracted much attention as a replacement for 'silicon technology' and offer the possibility of cheap, easily produced, photovoltaic energy from light. Naphthalocyanine and phthalocyanine possess good electron-donating properties due to their large easily ionized π-electron systems, whereas fullerene is good π-electron acceptor which can be bonded to other organic molecules. A naphthalocyanine–fullerene based supramolecular system is therefore a potential material for a photovoltaic cell due to its large and flexible absorption combined with electrical properties similar to those of an inorganic semiconductor.

Fig. 6 presents the chemical structure naphthalocyanine as a donor used in this study. These supramolecules have been reported in previous studies [37,38]. Many unimolecular

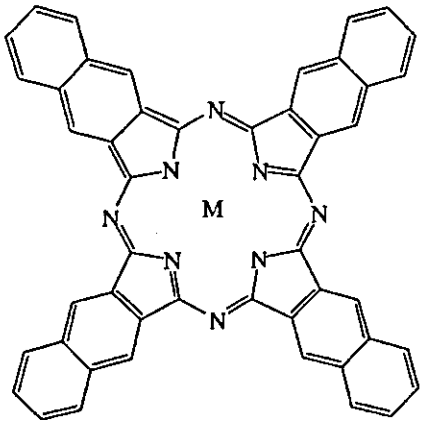

Fig. 6. Chemical structure of naphthalocyanine (M = 2H, free base naphthalocyanine, H2-Nc: M = Zn, zinc naphthalocyanine, Zn-Nc).

polymer–fullerene supramolecules have been synthesized for photovoltaic property [39]. These molecules have a σ-bond between the polymer and the fullerene to establish the localization of the frontier orbital. However, the above supramolecule have van der Waals bond instead of a σ-bond.

Fig. 7 shows the optimized structure of a naphthalocyanine–fullerene supramolecule using the HF/3-21G level.

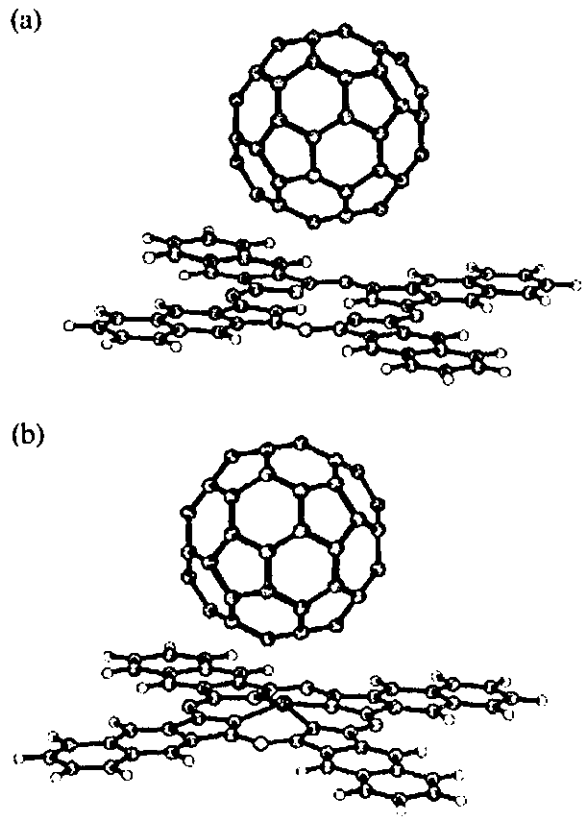

Fig. 7. Optimized structure of (a) a free base naphthalocyanine–fullerene supramolecule (H2-Nc + C_{60}) and (b) a zinc naphthalocyanine–fullerene supramolecule (ZnNc + C_{60}).

This structure contains the Zn atom in the low spin state. The planar structure of the free base naphthalocyanine is retained with fullerene, whereas, a slight bending is observed in zinc naphthalocyanine. The zinc atom is

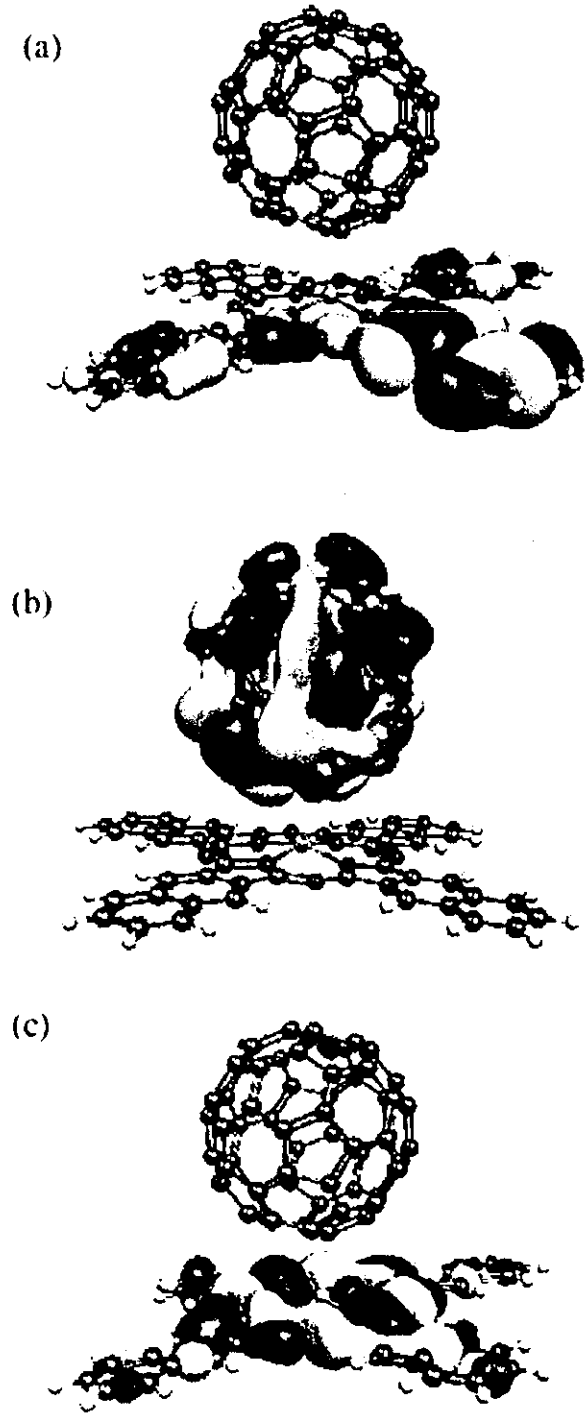

Fig. 8. Orbital spatial orientation of HOMO and LUMO + K (K = 0, 1, 2) in phthalocyanine–fullerene supramolecule. (a) HOMO, (b) LUMO, (c) LUMO + 3.

protruding from plane of the naphthalocyanine molecule to the side of fullerene. The distance between the zinc atom and the nearest carbon atom in fullerene is 2.54 Å. The zinc atom is the bridge site between six-member ring of the absorbed fullerene. We can observe the charge transfer from the fullerene to zinc naphthalocyanine while there is no charge transfer to free-base naphthalocyanine.

To estimate the electron transport through this molecule, we have analyzed the spatial distribution of the frontier orbitals (HOMO and LUMO), providing a strategy by which the photovoltaic properties of the naphthalocyanine–fullerene supramolecule can be understood. Fig. 8 indicates the spatial orientation for the molecular orbital spatial for the HOMO, LUMO, and LUMO + 3 energy levels of the naphthalocyanine–fullerene complex. It is clearly seen from Fig. 8 that for naphthalocyanine–fullerene supramolecule the LUMO is localized on the acceptor side, while the HOMO and LUMO + 3 is localized on the donor side.

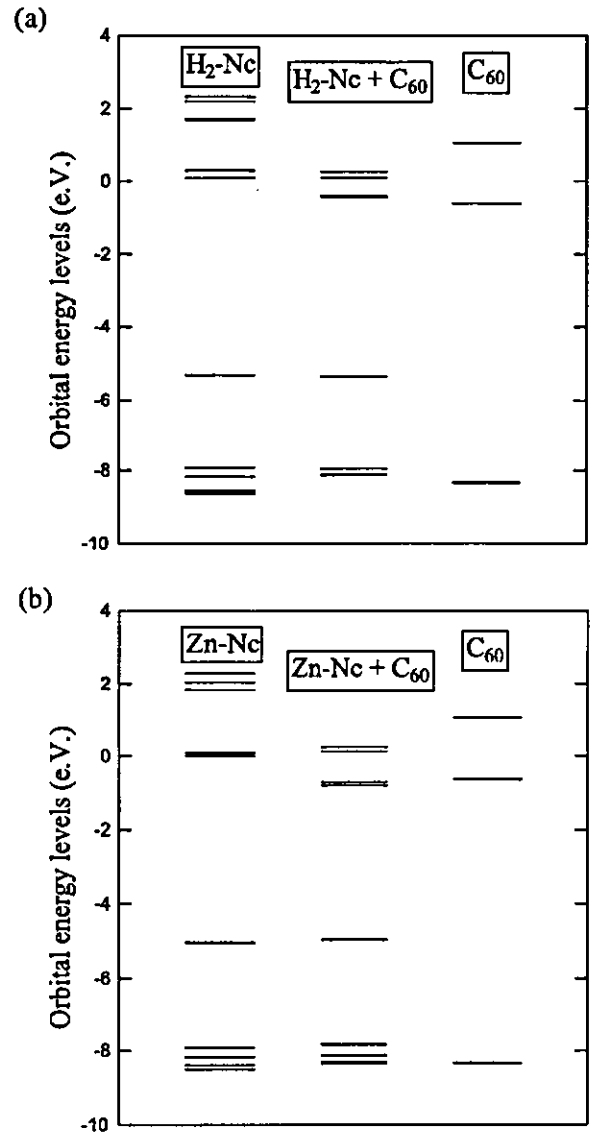

Fig. 9. Comparison of the five highest occupied and five lowest unoccupied orbital levels for Nc, Nc-C_{60} supramolecule, and C_{60}.

Fig. 9(a) and (b) compares the five highest occupied and five lowest unoccupied orbital levels for the optimized structure of the free base naphthalocyanine, fullerene, and the naphthalocyanine–fullerene supramolecule. It is interesting to note that the LUMO energy levels of the supramolecule compare well with the LUMO energy level of fullerene, and the HOMO energy levels of the supramolecule are close to the HOMO energy levels of the naphthalocyanine. It has been reported previously that the tendency for localization of the frontier orbitals of other donor–fullerene(acceptor) supramolecular systems is similar [40,41].

3. Conclusions

The geometry and electronic structure of molecules selected as candidates for application in molecular devices have been calculated using an ab initio approach. The electron transport in these molecules has been analyzed, based on the spatial distribution of the frontier orbitals. The localization of the unoccupied orbital state on the acceptor moiety mostly depends on the structure of the porphyrin polymer. From an application perspective, the polymer/fullerene mixture has attracted much attention as a potential candidate for organic solar cells due to its high efficiency. Regardless of whether there is a mixed structure, the donor and acceptor structure still remains. The calculated results for the electronic structure of a naphthalocyanine–fullerene supramolecule manifest that the HOMOs were localized on the donor sub-unit and the LUMOs were localized on the acceptor sub-unit. This research is continuing, and should be explored by employing more high accurate method and using a combinatorial approach.

Acknowledgements

The authors would like to express their sincere thanks to the Center for Computational Materials Science of the Institute for Materials Research, Tohoku University, for their continuous support of the HITAC SR8000-G1/64 supercomputing facilities. This study was performed through Special Coordination Funds for Promoting Science and Technology from the Ministry of Education, Culture, Sports, Science and Technology of the Japanese Government and a Grant for Basic Science Research Projects from the Sumitomo Foundation.

References

[1] A. Aviram, M.A. Ratner, Molecular rectifiers, Chem. Phys. Lett. 29 (1974) 277–283.

[2] A. de Silva, I.M. Dixon, H.Q.N. Gunaratne, T. Gunnlaugsson, P.R.S. Maxwell, T.E. Rice, Integration of logic functions and sequential operation of gates at the molecular-scale, J. Am. Chem. Soc. 121 (1999) 1393–1394.

[3] M.A. Reed, J. Chen, A.M. Rawlett, D.W. Price, J.M. Tour, Molecular random access memory cell, Appl. Phys. Lett. 78 (2001) 3735–3737.

[4] C. Joachim, J.K. Gimzewski, A. Aviram, Electronics using hybrid-molecular and mono-molecular devices, Nature 408 (2000) 541–548.

[5] Y. Huang, X.F. Duan, Y. Cui, L.J. Lauhon, K.-H. Kim, C.M. Lieber, Logic gates and computation from assembled nanowire building blocks, Science 294 (2001) 1313–1317.

[6] J. Chen, M.A. Reed, A.M. Rawlett, J.M. Tour, Large on–off ratios and negative differential resistance in a molecular electronic device, Science 286 (1999) 1550–1552.

[7] P.S. Damle, A.W. Ghosh, S. Datta, Unified description of molecular conduction: from molecules to metallic wires, Phys. Rev. B 64 (2001) 201403.

[8] J. Reichert, R. Ochs, D. Beckmann, H.B. Weber, M. Mayor, H.v. Löhneysen, Driving current through single organic molecules, Phys. Rev. Lett. 88 (2002) 176804.

[9] V. Mujica, A. Nitzan, S. Datta, M.A. Ratner, C.P. Kubiak, Molecular wire junctions: tuning the conductance, J. Phys. Chem. 107 (2003) 91–95.

[10] M.D. Vertra, S.-G. Kim, S.T. Pantelides, N.D. Lang, Temperature effects on the transport properties of molecules, Phys. Rev. Lett. 86 (2001) 288–291.

[11] M. Magoga, C. Joachim, Conductance of molecular wires connected or bonded in parallel, Phys. Rev. B 59 (1999) 16011–16021.

[12] S.N. Yaliraki, M.A. Ratner, Molecule–interface coupling effects on electronic transport in molecular wires, J. Chem. Phys. 109 (1998) 5036–5043.

[13] Y. Xue, S. Datta, S. Hong, R. Reifenberger, J.I. Henderson, C.P. Kubiak, Negative differential resistance in the scanning-tunneling spectroscopy of organic molecules, Phys. Rev. B 59 (1999) R7852–R7855.

[14] C. Majumder, H. Mizuseki, Y. Kawazoe, Molecular scale rectifier: theoretical study, J. Phys. Chem. A 105 (2001) 9454–9459.

[15] H. Mizuseki, K. Niimura, C. Majumder, Y. Kawazoe, Theoretical study of the alkyl derivative $C_{37}H_{50}N_4O_4$ molecule for use as a stable molecular rectifier: geometric and electronic structures, Comput. Mater. Sci. 27 (2003) 161–165.

[16] H. Mizuseki, N. Igarashi, C. Majumder, R.V. Belosludov, A.A. Farajian, Y. Kawazoe, Theoretical study of a donor–spacer–acceptor structure molecule for use as a stable molecular rectifier: geometric and electronic structures, Thin Solid Films 438–439C (2003) 235–237.

[17] R.V. Belosludov, H. Mizuseki, K. Ichinoseki, Y. Kawazoe, Theoretical study on inclusion complex of polyaniline covered by cyclodextrins for molecular device, Jpn. J. Appl. Phys. 41 (2002) 2739–2741.

[18] R.V. Belosludov, H. Sato, A.A. Farajian, H. Mizuseki, K. Ichinoseki, Y. Kawazoe, Molecular enamel wires for electronic devices: theoretical study, Jpn. J. Appl. Phys. 42 (2003) 2492–2494.

[19] R.V. Belosludov, H. Sato, A.A. Farajian, H. Mizuseki, Y. Kawazoe, Theoretical study of insulated wires based on polymer chain encapsulated in molecular nanotube, Thin Solid Films 438–439C (2003) 80–84.

[20] C. Majumder, H. Mizuseki, Y. Kawazoe, Bipyridinium molecular switch: ab initio electronic structure calculation, Mater. Trans. 42 (2001) 2276–2278.

[21] C. Majumder, H. Mizuseki, Y. Kawazoe, Theoretical analysis for a molecular resonant tunneling diode, Jpn. J. Appl. Phys. 41 (2002) 2770–2773.

[22] C. Majumder, T.M. Briere, H. Mizuseki, Y. Kawazoe, Molecular resistance in a molecular diode: a case study of the substituted phenylethynyl oligomer, J. Phys. Chem. 106 (2002) 7911–7914.

[23] J.Q. Lu, H. Chen, J. Wu, H. Mizuseki, Y. Kawazoe, Ab initio modeling of real molecular logic devices, Mater. Trans. 42 (2001) 2270–2275.

[24] C. Majumder, T.M. Briere, H. Mizuseki, Y. Kawazoe, Structural investigation of thiophene thiol adsorption on Au-nanocluster: influence of back bonds, J. Chem. Phys. 117 (2002) 2819–2822.

[25] C. Majumder, T.M. Briere, H. Mizuseki, Y. Kawazoe, Interactions of a conjugated molecular diode with small metal clusters of Cu, Ag, and Au: first-principles calculations, J. Chem. Phys. 117 (2002) 7669–7675.

[26] J.-T. Wang, H. Mizuseki, Y. Kawazoe, T. Hashizume, M. Naitoh, E.-G. Wang, S. Wang, Stability of Sb line structures on Si(001), Phys. Rev. B 67 (2003) 193307.

[27] A.A. Farajian, R.V. Belosludov, H. Mizuseki, Y. Kawazoe, Electronic transport though benzene molecule: effect of gold contacts, Physica E 18 (2003) 253–254.

[28] H. Chen, J.Q. Lu, J. Wu, R. Note, H. Mizuseki, Y. Kawazoe, Control of substituent ligand over current through molecular devices: an ab initio molecular orbital theory, Phys. Rev. B 67 (2003) 113408.

[29] A.A. Farajian, K. Esfarjani, H. Mizuseki, Y. Kawazoe, Electron-interaction effects on transport characteristics of nanotubes, Physica B 323 (2002) 242–243.

[30] A.A. Farajian, B.I. Yakobson, H. Mizuseki, Y. Kawazoe, Electronic transport through bent carbon nanotubes: nanoelectromechanical sensors and switches, Phys. Rev. B 67 (2003) 205423.

[31] GAUSSIAN98, Revision A.11.1, Gaussian, Inc., Pittsburgh PA, 2001.

[32] A. Tsuda, A. Osuka, Fully conjugated porphyrin tapes with electronic absorption bands that reach into infrared, Science 293 (2001) 79–82.

[33] R.M. Metzger, B. Chen, D. Vuillaume, M.V. Lakshmikantham, U. Hopfner, T. Kawai, J.W. Baldwin, X. Wu, H. Tachibana, H. Sakurai, M.P. Cava, Observation of unimolecular electrical rectification in hexadecylquinolinium tricyanoquinodimethanide, Thin Solid Films 327 (1998) 326–330.

[34] R.M. Metzger, J.W. Baldwin, W.J. Shumate, I.R. Peterson, P. Mani, G.J. Mankey, T. Morris, G. Szulczewski, S. Bosi, M. Prato, A. Comito, Y. Rubin, Electrical rectification in a Langmuir–Blodgett monolayer of dimethyanilinoazafullerene sandwiched between gold electrodes, J. Phys. Chem. 107 (2003) 1021–1027.

[35] G. Yu, A.J. Heeger, Charge separation and photovoltaic conversion in polymer composites with internal donor–acceptor heterojunctions, J. Appl. Phys. 78 (1995) 4510–4515.

[36] J.J.M. Halls, C.A. Walsh, N.C. Greenham, E.A. Marseglia, R.H. Friend, S.C. Moratti, A.B. Holmes, Efficient photodiodes from interpenetrating polymer networks, Nature 376 (1995) 498–500.

[37] Y. Zhao, L. Gan, D. Zhou, C.-H. Huang, J. Jiang, W. Liu, Photocurrent generation from a self-assembling guest-host LB film of C-$_{60}$(HOOCCHNHCHCOOH) and octopentyloxy phthalocyanine, Solid State Commun. 106 (1998) 43–48.

[38] T. Nojiri, M.M. Alam, H. Konami, A. Watanabe, O. Ito, Photoinduced electron transfer from phthalocyanines to fullerenes (C-60 and C-70), J. Phys. Chem. A 101 (1997) 7943–7947.

[39] S. Fukuzumi, H. Imahori, H. Yamada, M.E. El-Khouly, M. Fujitsuka, O. Ito, D.M. Guldi, Catalytic effects of dioxygen on intramolecular electron transfer in radical ion pairs of zinc porphyrin-linked fullerenes, J. Am. Chem. Soc. 123 (2001) 2571–2575.

[40] H. Mizuseki, N. Igarashi, R.V. Belosludov, A.A. Farajian, Y. Kawazoe, Theoretical study of chlorin–fullerene supramolecular complexes for photovoltaic devices, Jpn. J. Appl. Phys. 42 (2003) 2503–2505.

[41] H. Mizuseki, N. Igarashi, R.V. Belosludov, A.A. Farajian, Y. Kawazoe, Theoretical study of phthalocyanine–fullerene complex for a high efficiency photovoltaic device using ab-initio electronic structure calculation, Synth. Metals 138 (2003) 281–283.

Trends in
Photochemistry & Photobiology
Vol. 10, 2003

Spontaneous ultraweak photon emission of living organisms - biophotons - phenomena and detection techniques for extracting biological information

Masaki Kobayashi*
Department of Electronics, Tohoku Institute of Technology, 35-1, Yagiyama-Kasumicho, Taihaku-ku, Sendai 982-8577, Japan

ABSTRACT

Studies on the phenomenon of spontaneous ultraweak photon emissions observed from living organisms are reviewed. A novel technology for the detection of very low levels of light and the analysis of spatial, temporal, spectral and photon statistics will be explained. Experimental results obtained through photon emission imaging of rat brains, mouse bodies and human body surfaces are discussed in terms of their mechanisms and of feasibility studies for biological and medical applications.

1. INTRODUCTION

Faint lights glowing in the dark, such as the blinking of fireflies, are very attractive. When bioluminescence is observed in living organisms, it seems fantastic and it stirs our curiosity. However, if we were to have extremely sensitive eyes that could detect a single photon, we would find that all of the living organisms in the world are actually shining like fireflies. Luminescence from living organisms is not a phenomenon that only applies to specific species such as fireflies, but is a general property that is possessed by all organisms. These emissions are ultraweak in intensity, with a range far removed from that of fireflies, and nobody can see them with the naked eye, although the phenomenon can be observed using highly sensitive photon detectors. The development of the photomultiplier tube in 1950s has gradually allowed these photon emission phenomena to be revealed [1]. Terms such as ultraweak photon emission and spontaneous ultraweak, low-level, or dark bio-/chemi-luminescence, etc. are now in general use to describe these phenomena, in order to distinguish them from general bioluminescence. The concept of the biophoton [2] is also commonly used to represent these phenomena. In this review, technologies for the determination and analysis of biophotons and several studies (chiefly based on the imaging of biophotons) for biological and medical applications aimed at diagnostic use are described.

In the last half-century, several studies have been carried out to explore various aspects of biophotons that have been observed in different organisms, particularly for the elucidation of their mechanisms and for the development of practical applications. Although a great deal of knowledge has been accumulated regarding biophoton phenomena, the weak intensity of the emissions has restricted the practical application of biophoton technology to just a few limited fields. In order to make further progress in the development of biophoton applications, sophisticated techniques for analyzing the faint emissions from a restricted number of photons are required. We have continued studying the

*e-mail: masaki@tohtech.ac.jp

biophoton from a variety of viewpoints in the fields of biophysics, biochemistry, and biomedical engineering, and we have contributed to advances in the interpretation of their mechanisms and the development of applications, including analysis methods and instrumentation [3]. Here, I will review the modern technology used for biophoton analysis and also feasibility studies for a wide range of subjects to determine if there is any useful pathophysiological information that they can convey.

The following instrumentation systems are described: (1) A highly-sensitive photon counting apparatus designed for the improvement of long-term stability. (2) A biophoton imaging apparatus for spatiotemporal analysis based on a two-dimensional photon counting technique. (3) An imaging apparatus using a highly sensitive charge coupled device (CCD). (4) An apparatus for the spectral analysis of biophotons using a set of colored-glass filters with a wide range of wavelengths covering from the ultraviolet to the near infrared regions. (5) An apparatus for determining photon statistics and photon correlation characteristics based on a method that traces single-photon pulses from a detector.

In terms of feasibility studies for biomedical applications, experimental results obtained from the measurement of plants and mammals through imaging and spatiotemporal characterization to clarify the relationship between biophotons and pathophysiological responses are described and discussed as follows. (1) The responses of plants to exogenous stress. (2) Determination of the spatiotemporal propagation of pathological responses under induced oxidative stress observed on a mouse body. (3) Biophoton emission from the brain of a rat that is associated with observed neuronal activity. (4) Biophoton imaging of a human body. (5) Characterization of oxidative stress through the spectral analysis of samples originating from human subjects. In addition, (6) experiments for the extraction of information through the analysis of photon statistics are also discussed, which indicate a method for the characterization of intercellular communication in the development of microorganisms.

2. DETECTION AND ANALYSIS TECHNIQUE OF BIOPHOTONS

2.1 PHOTON COUNTING [4]

We have developed newly designed photon counting system for the measurement and analysis of ultraweak photon emission to improve the performance of long-term stability. Figure 1 shows a block diagram of the system and a schematic illustration of the detector housing. A photomultiplier tube (PMT) is installed in an inner chamber filled with pure nitrogen; this chamber is arranged in a vacuum cryo-chamber attached to a pair of pulse tube refrigerators (Cryo-Mini; Iwatani Gas Co., Tokyo, Japan). The cold heads of the refrigerator are connected to the inner chamber and the PMT photocathode can be cooled to below –80°C and controlled with an accuracy of ±0.1°C. The detector housing was designed for PMTs of the head-on type with photocathodes measuring 46 mm in diameter.

We have evaluated several PMTs in model R1333 (Hamamatsu Photonics), which was designed for photon counting applications with a red extended multi-alkaline phtochathode, to characterize the statistical properties of dark count for selection of the superior tube. A breeder circuit is incorporated in the PMT socket, which is made of ceramics (model E678-21D; Hamamatsu Photonics, used for PMT model R1333) for use under cooling, and the output signal of the PMT is fed into a constant-fraction discriminator (model 583; EG&G ORTEC) via a 150-MHz preamplifier. A power supply with high stability and low ripple (model HESX-3R5; Matsusada Precision Inc., Shiga, Japan) is used for providing high voltage of the PMT. Photoelectron pulses are fed into a photon-counter (SR400, Stanford Research Inc., USA) and simultaneously into the specially designed pulse-interval counter to consecutively record pulse-to-pulse intervals.

The lower discriminator level is determined by the pulse-height distributions measured with varying PMT high voltage to maximize the signal-to-noise ratio. In the case of our selected PMT, the averaged number of dark counts is 12.5 counts/s with cooling at –40°C. The quantum efficiency of the photocathode is 4.8% at 650 nm with a spectral sensitivity from 400 to 900 nm. The

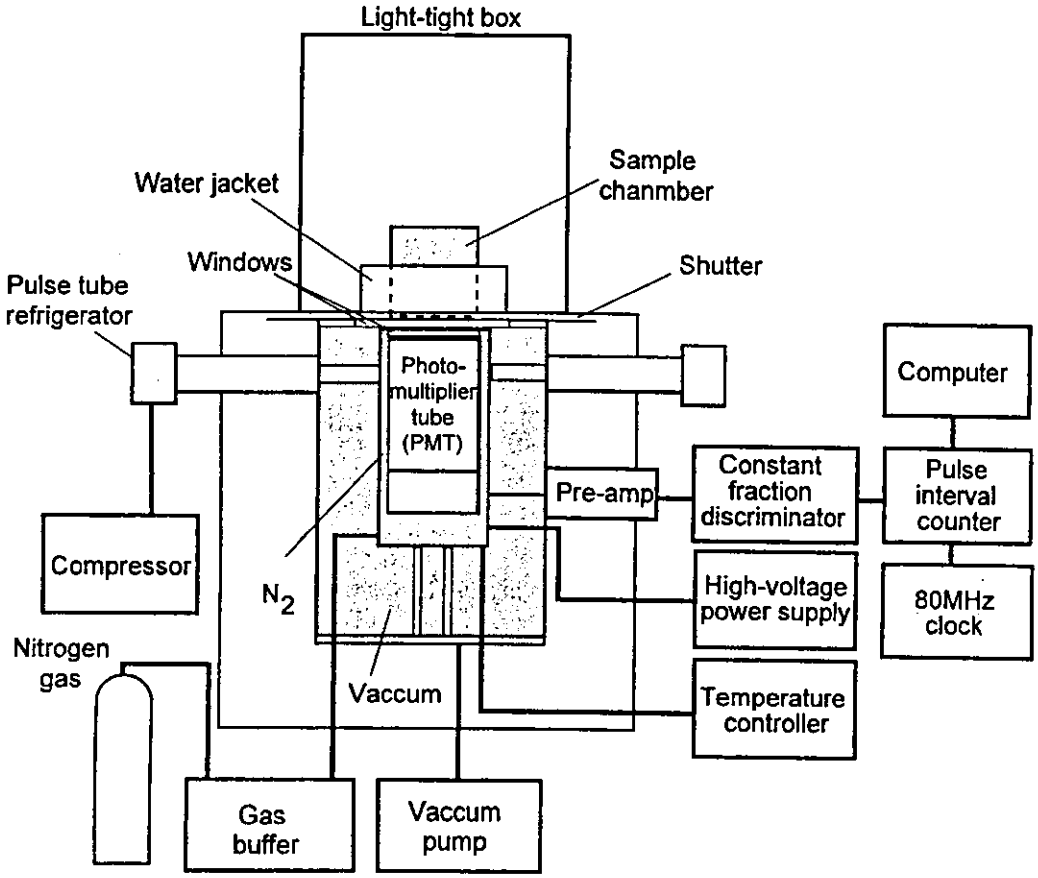

Fig.1 A block diagram of a highly sensitive photon counting system.

distance between a sample to be measured and the photocathode of the PMT is 18 mm via double quartz windows and no lenses are used. Consequently the light-collection efficiency is estimated to be 33%. The minimum detectable optical radiant flux density was estimated to be 6.25 x 10^{-18} W/cm^2 in an observation time of 1 s, which was evaluated experimentally using an integral sphere under the wavelength condition of 650 nm, which denotes that a single photoelectron corresponds to 52 photons emitted on the sample surface.

Figure 2 demonstrates the long-term stability of the system expressed by the time course of dark counts (a), and its power spectrum (b) obtained from an averaged 10 independent measurements. This result shows that the PMT dark current does not depend on the frequency (white noise) in the region above approximately 2x10^{-5} Hz, indicating shot noise of thermoionic emission. However, the power spectral density in the frequency region below 2x10^{-5} Hz is recognized as bearing 1/f characteristics, which can be speculated to be derived from the 1/f fluctuation of load resistance, considering the stability of temperature of the photocathode and the supplied high voltage.

2.2 PHOTON COUNTING IMAGING AND SPATIOTEMPORAL ANALYSYS [5, 6, 7]

The imaging system for biophoton emission developed

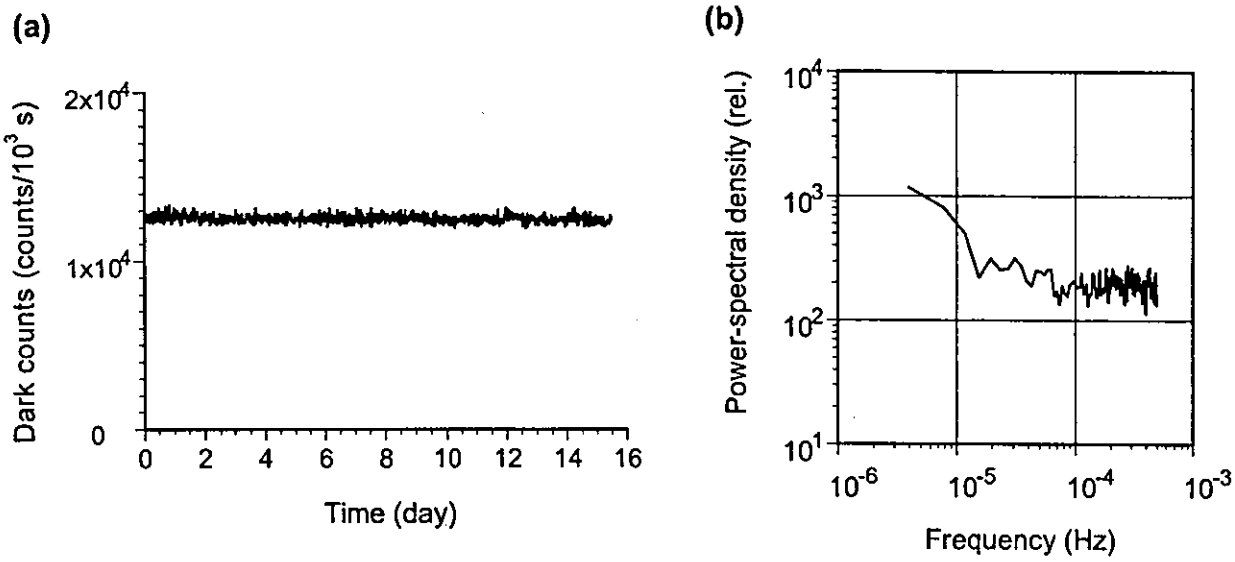

Fig.2 An experimental result evaluated long-term stability. (a) Time course of dark counts. (b) Power spectral density of the dark count variation.

in our group consists of a two-dimensional photon counting tube with a large active area, a highly efficient lens system installed in a sample chamber, and an electronic apparatus for identifying the two-dimensional spatial and temporal photoelectron information. A block diagram is shown in Fig. 3. The photon counting tube (Model IPD 440, Photek, Ltd., UK), which was installed in the vacuum chamber, had a photocathode measuring 40 mm in diameter with spectral sensitivity (S-20) operating at a wavelength ranging from 350 to 900 nm, and with a quantum efficiency of 9% at 500 nm, 5.5% at 600 nm, and 1.3% at 800 nm.

The tube dark count was less than 76 counts/s over the whole effective area with cooling at –35°C. Spatial resolution of the tube, which was determined by the readout precision of the resistive anode incorporated into the photon counting tube, was approximately 200 μm.

A specially designed lens system (Fujii Optical Co., Tokyo, Japan) had a 90 mm aperture with a 0.5 N.A. (numerical aperture) and 1.0 magnification corresponding to an image size of 25 by 25 mm or 1/3 with 75 by 75 mm image size. Output pulses from the resistive anode were fed to a position computer (IPD controller, Photek) to determine the X-Y position of each photoelectron event. These data (9 bits, 2 channels) were consecutively transferred to a pulse- interval counter (Tohoku Electronic Industrial Co., Sendai, Japan) and stored with timing data of the event, which is represented as the time interval between two successive photoelectron pulses. The time resolution of events is restricted by the position-computer to a pulse-pair resolution of 10 μs.

After data acquisition, the data were transferred to a workstation for reconstruction of the photon counting images and analysis of spatiotemporal properties, which demonstrated the intensity kinetics in regions of interest or space-time correlation of the photoelectrons.

Images were processed with data correction for the spatial distribution of dark counts and Gaussian smoothing. Spatial resolution on the processing was adapted with the sample intensity. Minimum detectable radiant flux density, which was defined with dark counts from the detector, quantum efficiency of the photocathode, photoelectron collection efficiency, and light collection efficiency of the lens system, was experimentally evaluated and found to be 9.90×10^{-17} W/cm^2 (= 314 photons/s·cm^2 at a wavelength of 670 nm) under the condition of spatial resolution of 2.3mm in the

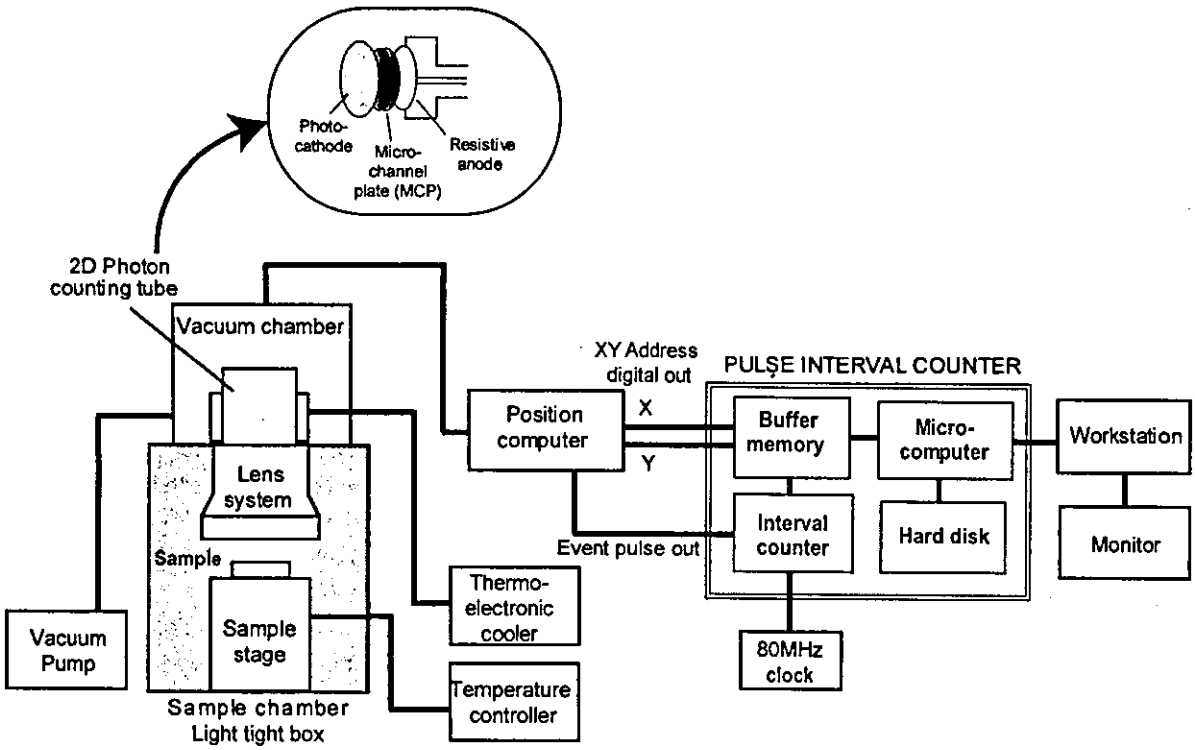

Fig. 3. A block diagram of biophoton imaging system characterized with a highly sensitive imaging and spatiotemporal analysis for biophoton emission. Timing pulses in photoelectron event from a position computer operate a pulse counter to measure pulse-to-pulse interval based on an 80 MHz clock. Time interval data and position data are transferred to a buffer memory and finally stores in a hard disk continuously.

case of 1.0 magnification. A single photoelectron of the detector was estimated to correspond to 221 photons emitted onto the sample surface.

Raw data accumulated in the pulse interval counter are expressed by a set of sequences $\{(x_1, \xi_1), (x_2, \xi_2), ..., (x_N, \xi_N)\}$, where ξ_i is the arrival time-interval between the $(i-1)$-th and the i-th photoelectron and x_i is the two-dimensional location of the i-th photoelectron; and N is the total number of photoelectron pulses. Initially, a photon counting image, expressed as $n(x, y)$, which is the number of photoelectron pulses at position (x, y) during a total measurement period, is constructed. After setting regions of interest ($r_j = \{[x_{j1}, x_{j2}], [y_{j1}, y_{j2}]\}$) on the image plane, the number of photoelectron pulses per unit time T (observation time) in each region are calculated as $n(r_j, t, T)$ to extract the intensity time course. The spatial and temporal correlations of emission intensity $\langle I(r_1,t)\ I(r_2,t+\tau)\rangle$ are calculated from the photoelectron correlation that is derived from the photoelectron detection probability at a space-time point (r_1, t) and detection probability after time τ at r_2, represented by the conditional probability $P_c(r_2, \tau)$ of two successive photoelectron pulses. The relationship is expressed as

$$\langle I(r_1,t)\ I(r_2,t+\tau)\rangle = \alpha \langle n(r_1,t,T)\rangle P_c(r_2,\tau)$$

where the brackets < > denote ensemble averaging and α, a constant.

The advantage of this system is the arbitrary selection of spatial and temporal dimensions (r_j and T, τ), which can be achieved from a single measurement data point instead of making a fresh measurement for each change in the spatial or temporal dimensions.

2.3 CCD IMAGING [8]

A highly sensitive CCD camera system cooled with liquid nitrogen or closed-cycle mechanical cryogenic cooler incorporated with a thinned back-illuminated type CCD is also available for biophoton imaging. The imaging format of CCD (TK1024AB2-G1; SITe, OR, USA) used in our experiments incorporated in CCD camera system (ATC200C; Photometrics, Arizona, USA) was 1024 x 1024 pixels for a full frame with each pixel size being 24 x 24 μm. Dark current of the device is 0.225 e^-/hr·pixel (= 6.25×10^{-5} e^-/s·pixel) at –120°C in MPP (multi- phase pinned) mode and the readout noise is 3.3 e^- RMS/pixel. In the experiments, according to the intensity of the emission, spatial resolution of the CCD is regulated with binning mode. Quantum efficiency of the system is 73% at 700 nm. In comparison with the two-dimensional photon counting system, selection of a suitable imaging device according to the emission spectrum and integration time that depends on the emission intensity is necessary for optimum imaging of biophotons. Recently, the advancement of a highly-sensitive cooled CCD camera system is remarkable. It is also available the system which has a mechanical cryogenic cooler without using liquid nitrogen.

2.4 SPECTROSCOPY [9]

For spectral analysis of biophoton, we have developed the spectral analyzing system for ultraweak photon emission over a wide range of wavelength. Two models of PMT with different spectral responses selected for highly sensitive detection under the operation of single photon counting are used. The designed system for filter-spectroscopy is suited to the properties of biophoton emission because of a broad spectrum and little need for high resolution of the wavelength in comparison with demand for high sensitivity [10]. Colored glass filters that have long-path and sharp cut-off characteristics in wavelength are used. In our studies, a set of 37 filters, with different cut-offs, from 250 to 850 nm was used. Spectral distribution of the sample was calculated as the difference between transmitted intensities of two subsequent filters. The block diagram of the system is indicated in Fig.4 (a). A flowchart of the process of the computation procedure to derive the spectral distribution are shown in Fig.4 (b) with a schematic illustrations displayed in Fig.4 (c). The system has two detectors with different spectral responses for over a wide range of measurements. A PMT of R1333 is used for the range of 300-900 nm and an R375 is for 160-650 nm. Filters are mounted on a rotating disk inserted between the sample chamber and the PMT. One cycle of the rotating disk provides a set of transmitted intensity data through all filters including the dark count of the PMT and total intensity over the wavelength range that is measured without any filters. An illustrated figure of raw data obtained with repeated disk cycles is shown in Fig.4(c)-A with temporal changes of the total intensity and dark count acquired in each rotation (Fig.4(c)-B). After subtraction of the background emission of the filters, correction of temporal changes of the total intensity and dark count are carried out. Integration of the intensity obtained for each filter is then calculated as shown in Fig.4(c)-C. Fig.4(c)-D is the result after calculating the difference between subsequent data. Correction of spectral response (Fig.4(c)-E) of the PMT is also applied, and then the spectral distribution is expressed as a histogram, as shown in Fig.4(c)-F, with the wavelength resolved by the cut-off properties of each filter. For visualization, if necessary, the spectral distribution can be displayed as a curve as shown in Fig.4(c)-H through convolution treatment using a window-function for the filters (Fig.4(c)-G), which is obtained by subtraction of the transmittance curves from two subsequent filters. Consequently, the wavelength resolution of the system is approximately 20-30 nm through the range 300-700 nm and 30-50 nm in the other wavelengths region.

2.5 BIOPHOTON STATISTICS ANALYSIS [4, 11]

We have explored novel technique for the measurement and analysis technique determining the fluctuation of ultraweak photon emission field. Measurements were performed with the single photoelectron counting technique, using a PMT based on a continuous and sequential measurement of the time intervals between

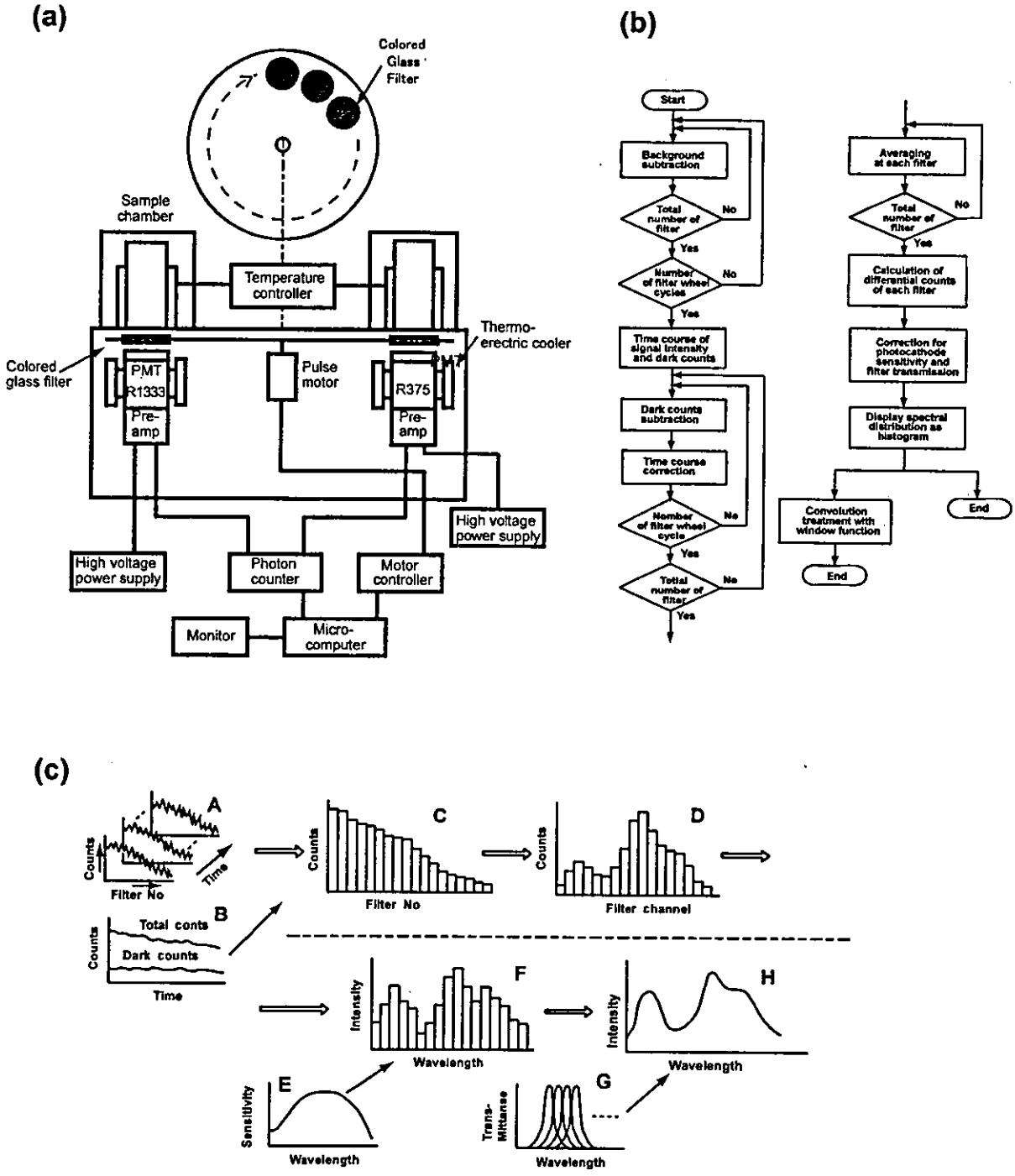

Fig. 4 .(a) A block diagram of the spectrum analyzing system that is incorporated with two different type of PMTs. (b) A flowchart indicating the procedure of measurement and analysis. (c) A schematic illustration of procedure to determine a spectrum with the spectrum analyzing system.

two successive photoelectron pulses. Based on the raw data of pulse intervals, the Fano factor [$F_n(T)$; variance over mean of the number of photoelectrons observed within observation time T] is computed as an indicator for photon counting statistics, which quantifies the deviation from Poisson statistics as a function of observation time T. For data processing, corrections are necessary for correlative components intrinsically accompanying the PMT dark pulses that are caused by cosmic-ray-induced photoelectron clusters and micro-discharges occurring in the PMT. Because the afterpulse effects initiated by the incident photons are negligible under our conditions, we found that the photoelectron pulse events originating from incident light and the correlative components of dark pulses are statistically independent. Consequently, the Fano factor of incident light is deduced by subtracting the variance of the dark component, which had previously been measured, from that of the observed data.

For the data processing deriving the Fano factor, $F_n(T)$, which is defined by the variance over the mean of the number of photoelectrons within the observation time T, provides information of the intensity correlation of the optical field, indicating deviations from Poisson statistics as a function of observation time T . The correlative component of PMT dark counts is also corrected based on statistical independence. The Fano factor of incident light is consequently deduced by subtracting the variance of the dark component, which had previously been measured, from that of the observed data.

Under the stationary optical field, when the number of photoelectrons and dark events from the PMT in the t_i -th time period with observation time T are represented by $n_s(t_i, T)$ and $n_d(t_i, T)$, respectively, and their averages per unit time are indicated as μ_s and μ_d, and the average of total events as μ, these parameters are

$$\mu_s = \langle n_s \rangle / T \qquad (1)$$

$$\mu_d = \langle n_d \rangle / T \qquad (2)$$

$$\mu = \mu_s + \mu_d \qquad (3)$$

where $\langle \cdots \rangle$ denotes an ensemble average. The variance of photocounts n with observation time T, represented as $\langle \Delta n^2 \rangle$, is

$$\langle \Delta n^2 \rangle = \langle (n(T) - \mu T)^2 \rangle \qquad (4)$$

From the independence of events (i.e., the incident light and the dark components) $\langle \Delta n^2 \rangle$ is expressed, using variances $\langle \Delta n_s^2 \rangle$ and $\langle \Delta n_d^2 \rangle$, as

$$\langle \Delta n^2 \rangle = \langle \Delta n_s^2 \rangle + \langle \Delta n_d^2 \rangle . \qquad (5)$$

The Fano factor of the optical field is given as

$$F_n(T) = \frac{\langle \Delta n^2 \rangle - \langle \Delta n_d^2 \rangle}{\mu_s T} . \qquad (6)$$

In the case of a nonstationary optical field, when the time course of intensity can be expressed as a function of time, the variance is calculated from the following equations by using the intensity as a function of time $I(t)$. Eqs. (1) and (3) are expressed as time functions

$$\mu_s(t) = \langle n_s(t, T) \rangle / T = I(t) \qquad (7)$$

$$\mu(t) = \mu_s(t) + \mu_d . \qquad (8)$$

Here we define the variance of photocounts n, $\langle \Delta n^2 \rangle$, throughout the total measurement time T_M, as

$$\langle \Delta n^2 \rangle = \frac{1}{T_M} \int_0^{T_M} \{(n(t,T) - \mu(t)T\}^2 dT . \qquad (9)$$

Consequently, the Fano factor of the optical field is derived by

$$F_s(T) = \frac{\langle \Delta n^2 \rangle - \langle \Delta n_d^2 \rangle}{\frac{1}{T_M} \int_0^{T_M} I(t) T dt} . \qquad (10)$$

In the case when $I(t)$ was not given analytically, we define it by the moving average of observed data, which is represented as

$$I(t_i) = \frac{1}{T_a} \sum_{k=i-j/2}^{k=i+j/2} n(t_k, T_a) - \mu_d . \qquad (11)$$

Here $j\,T_a$ ($>> T$) is determined by the frequency at which the power spectral distribution of $n(t_i, T_a)$ changes from frequency-dependent to frequency-independent. The Fano factor is hence written as

$$F_n(T) = \frac{\langle \Delta n^2 \rangle - \langle \Delta n_d{}^2 \rangle}{\frac{1}{N}\sum_{i=1}^{N}\left(\frac{T}{T_a}\sum_{k=i-j/2}^{i+j/2} n(t_k, T_a)\right) - \mu_d T}, \quad (12)$$

where

$$\langle \Delta n^2 \rangle = \frac{1}{N}\sum_{i=1}^{N} (n(t_i, T) - I(t_i)T)^2$$

$$= \frac{1}{N}\sum_{i=1}^{N}\left(n(t_i, T) - \frac{T}{T_a}\sum_{k=i-j/2}^{i+j/2} n(t_k, T_a) + \mu_d T\right)^2$$

3. CHARACTERIZATION OF BIOPHOTON PHENOMENA FOR BIOLOGICAL MEASUREMENTS AND APPLICATIONS

Biophoton emission originates in the electronically-excited states of the constituents of living cells, which are generally associated with the presence of an oxidative metabolism that accompanies the production of reactive oxygen species (ROS). During the normal energy metabolism, cellular respiration (a reaction in the electron transfer chain of the inner mitochondrial membrane) participates in ROS production, which is especially facilitated under the highly-reduced state of an electron transfer chain.

Biophoton emission reflects the pathophysiological state with respect to energy (ATP) production and the susceptibility to oxidative stress, which is derived from the excessive production of ROS or a lack of activity for antioxidant protection. Ultraweak photon emission at the subcellular level, such as that from isolated mitochondria [12, 13, 14] and at the cellular level, such as that from cultured carcinoma cells [15, 16, 17] suggest a relationship between photon emission intensity and metabolic activity. Boveris et al. characterized photon emissions from a variety of mammalian organs in an in vivo investigation of the reactions of radicals through lipid peroxidation. Many pioneering studies have suggested the potential usefulness for noninvasive monitoring of oxidative metabolism and oxidative damage to living tissue [18, 19] under physiological and pathological conditions.

In this section, I will describe feasibility studies for biological measurements to extract physiological or pathological information for various subject organisms.

3.1 PLANTS [5]

The determination of the physiological responses of plants has been studied through the analysis of the spatiotemporal properties of biophotons. We analyzed the biophoton responses from a soybean root under various external stimulations. Here, I show a typical result that was observed for the response after stimulation by root tip excision.

In Figure 5 (c), the variation of the biophoton emission on excision of the root tip is displayed as the time courses of the intensity in the selected regions defined in Fig. 5 (a), which shows the integrated image over the total measurement time of 5 hours. The emission intensity of the cut region (Fig.5 c #1) increases and remains at a high level for 3 hours. Significant changes in photon emission intensity were observed at a remote position (Fig.5 c #10). The manifestation of a response to injury by the soybean seedling via an increase in photon emission at a position remote from the injury site is attractive. This region, referred to as the hypocotyls, is known to be highly active in cellular respiration; therefore the temporary enhancement of photon emission is suggested to be a reflection of increased metabolic activity connected to cellular respiration induced by the external stimulation. It is suggests that the biophoton emission from a mechanically-injured soybean root involves a contribution from the endogenous H_2O_2-peroxidase system [20, 21], and it is postulated that the phenomenon reflects a defensive response within the plant to seal off the wound and to generate new tissue for wound-healing through the activation of the peroxidase system.

This demonstrates the potential usefulness of the dynamics analysis of biophotons to monitor the response of a living system to environmental stimuli. Reactions occurring at a remote site may indicate the holistic

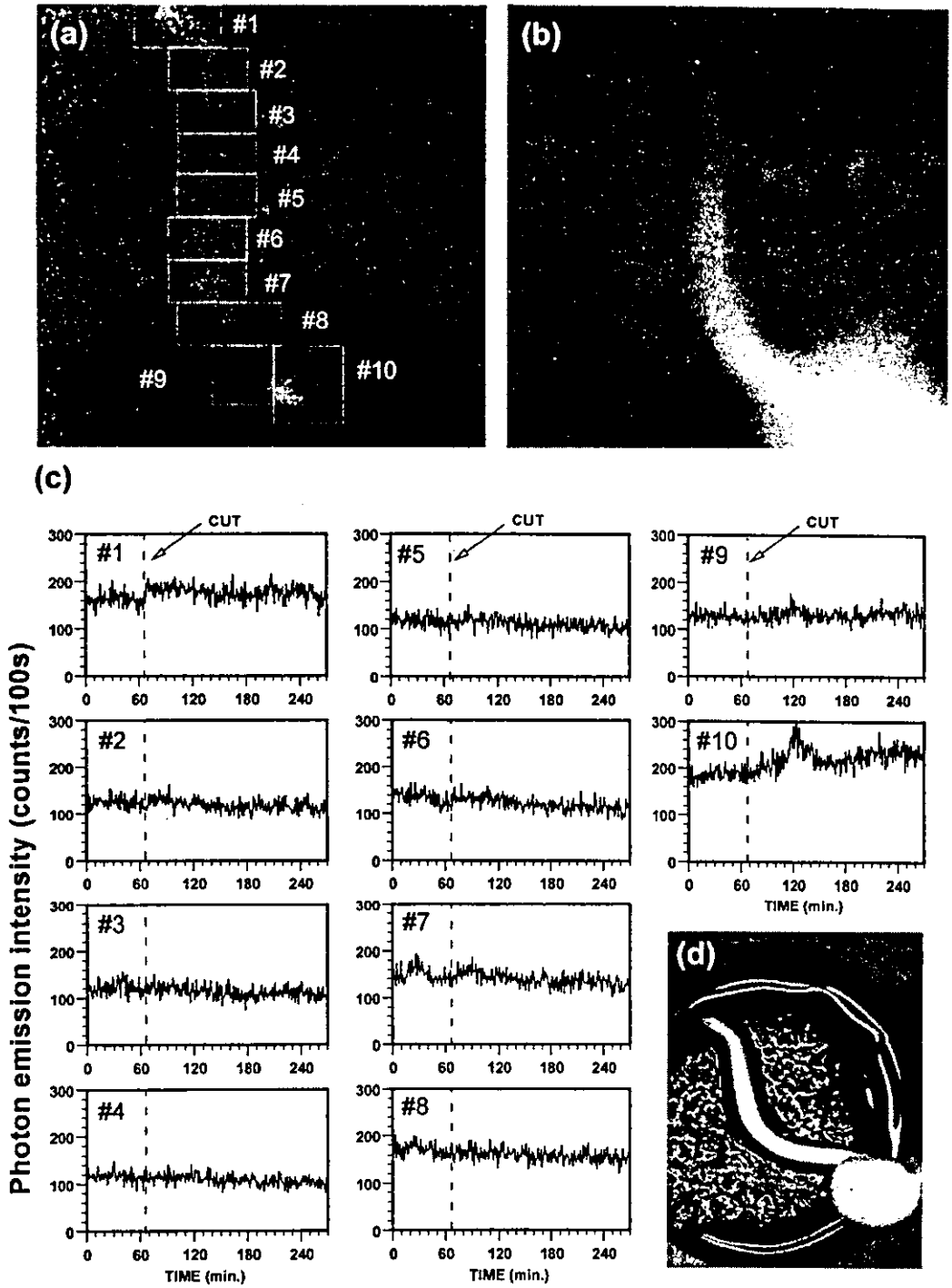

Fig. 5. Spatiotemporal variation of biophoton observed after stimulation of root-tip excision of soybean under germination. (a) Biophoton image obtained with integration time of 4.5 hours. (b) Image of the sample taken under weak light illumination. (c) Time courses of biophoton emission intensity in different regions indicated as white squares on the Fig.5 (a). (d) The photograph of the sample after the measurement.

response of the plant. Living systems maintain a complex order, both at the cellular level and at the macroscopic level. It is natural to assume that any form of external stimulus, be it physical, chemical or pathological, would disturb this order and manifest itself at different locations. The results of our present study show that our method could add a new dimension to the non-invasive study of the response of plants to injury or diseases, and could also contribute to the study of mechanisms for signal transfer within a living system.

3.2 MAMMAL [22]

We have attempted to establish a technique whereby pathophysiological information in mammals can be visualized in vivo based on biophoton imaging. Determination of the spatiotemporal distribution of biophotons using a two-dimensional photon counting technique could also provide the kinetics of the pathological and/or physiological states. Here, I will introduce some experiments that were carried out using mice to visualize the spatiotemporal propagation of oxidative stress and oxidative injury occurring in internal organs.

Paraquat is known to generate superoxide through the radical reaction of paraquat ions with oxygen, and its ingestion induces oxidative injury of the internal organs. We examined the changes in the biophoton images observed on the body surface after the administration of paraquat. A nude mouse was placed in the sample chamber under anesthesia. After the oral administration of paraquat, its biophoton image was observed in the supine position for 15 hours. Figure 6 shows a typical result, indicating the temporal changes of the biophoton images. Figures 6 (a)–(c) represent the images observed at 2, 5, 7 hours after administration respectively, with 1 hour integration. The small graphs in Fig. 6 (d) represent the spatiotemporal characteristics of the biophoton emission expressed with the temporal changes of the

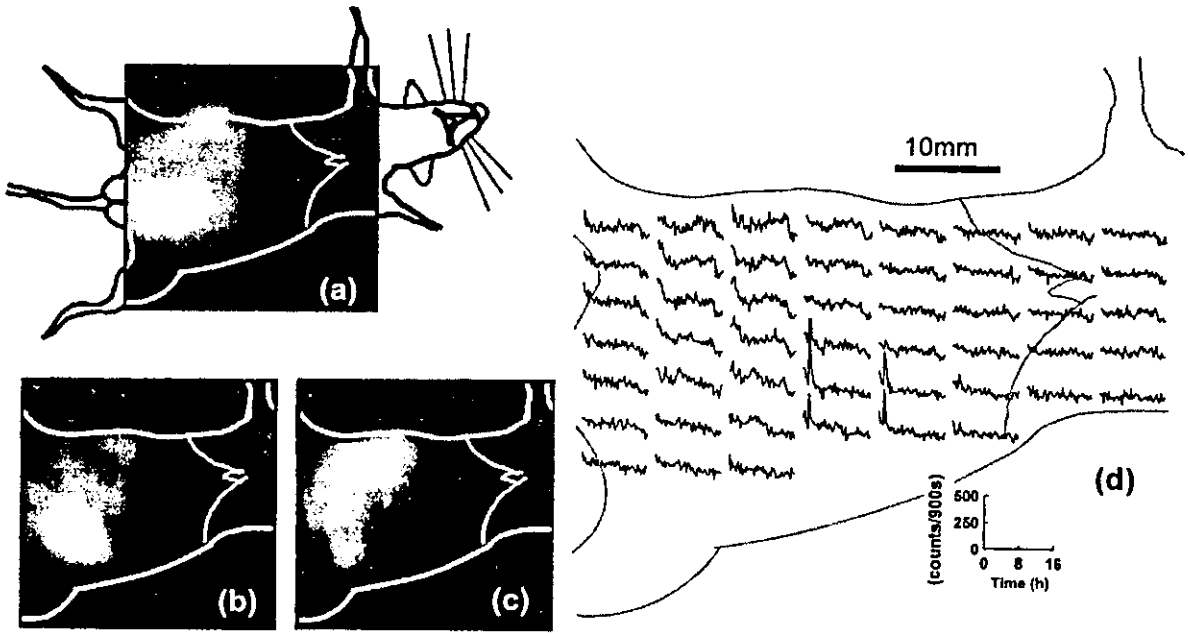

Fig. 6. Spatiotemporal analysis of biophoton emission of a mouse under oxidative stress induced by paraquat administration. (a) An image obtained 2 hours after the administration. (b) 5 hours after the administration. (c) 7 hours after the administration. (d) Spatiotemporal properties of biophoton intensity. Each graph shows time course of emission intensity at the indicated position. All images of biophoton were taken with 1-hour integration.

intensity with a time resolution of 15 minutes for each region, which were divided into the positions indicated on the profile of the mouse body. The results indicate a distinctive augmentation of the intensity centered on the area corresponding to the stomach 2-3 hours after administration and at the intestine after 5-10 hours. Control experiments using untreated mice under normal conditions showed no remarkable changes in the intensity distribution over the same period. This augmentation of the intensity implies the propagation of the affected part by oxidative injury. We also examined the site of origin of the photon emission to determine whether or not it originated inside the body, i.e., in the internal organs. We found that the majority of the detected photons were derived from the internal organs and/or the hypodermis, with a lesser contribution from the skin surface.

Microscopic observations of cellular damage to tissue that was removed from the sacrificed mouse after the measurement showed damage to the mucous membranes in the stomach and in the intestine. Although analysis in detail is necessary for pathological diagnosis, the preliminary results derived from these experiments suggest the potential for the application of spatiotemporal analysis of biophotons in pharmacokinetic and pathological investigations. For example, it may applicable to the assessment of oxidative stress induced by adverse reaction to a drug.

Biophoton imaging was also studied in cancer-transplanted mice. Significant enhancement of the emission intensity was observed according to the growth of the tumor, indicating that it correlated with the growth rate and viability of the cancer cells [17, 23]. This observation offers a valuable application for the evaluation of malignancy and for pharmacological studies on the effects of anti-cancer drugs.

3.3 RAT BRAINS [7]

In this section, two-dimensional imaging of the biophoton emission from a rat's brain, detected in vivo over the skull, is demonstrated. The physiological properties of the emission associated with metabolic activity, through simultaneous measurement of electroencephalographic (EEG) activity, are described. Analyses of the mechanisms of photon emission are also presented by using spectral analysis of in vitro brain slices.

3.3.1 Correlation between photon emission intensity and EEG activity

Biophoton imaging of rat's brain bas performed under anesthesia and artificial ventilation. After the incision of skin to exposure the skull, measurements have been carried out, under the atmospheric condition of nitrogen to eliminate the artificial chemiluminescence by autooxidation of the exposed tissue surface, with various physiological conditions. An example of the time course of biophoton emission intensity and simultaneously measured EEG activity represented by the theta wave component of the EEG power spectrum is displayed in Figure 7 (a). Temporal changes of the photon emission intensity were relatively comparable to the theta wave activity. Changes in the spatial pattern of emission were also observed from images in the respective time regions, as shown in Fig. 7 (b).

Figures 8 (a) and (b) show the results of correlation analysis between photon emission intensity and theta wave activity, represented by 30-minute integration under a different condition of skull treatment. Figure 8 (a) shows the result obtained from four animals where the parietal bones were removed and (b), that obtained over the skull from eleven animals. Both figures have been composed by superimposing independent measurements. Although emission intensities observed through the skull are approximately one-half of those with the parietal bones removed, both results support the correlation between photon emission intensity and the theta wave component of the EEG power spectra, with statistical significance ($p<0.001$). This result implies the relationship between biophoton emission intensity and metabolic activity of neural cells as interpreted with expression of energy metabolism.

3.3.2 Ultraweak photon emission spectra of brain slices

In order to elucidate the mechanism for biophoton emission from a rat's brain, we have performed spectral analysis of extracted brain slices. The slices were prepared after decapitation under diethyl ether

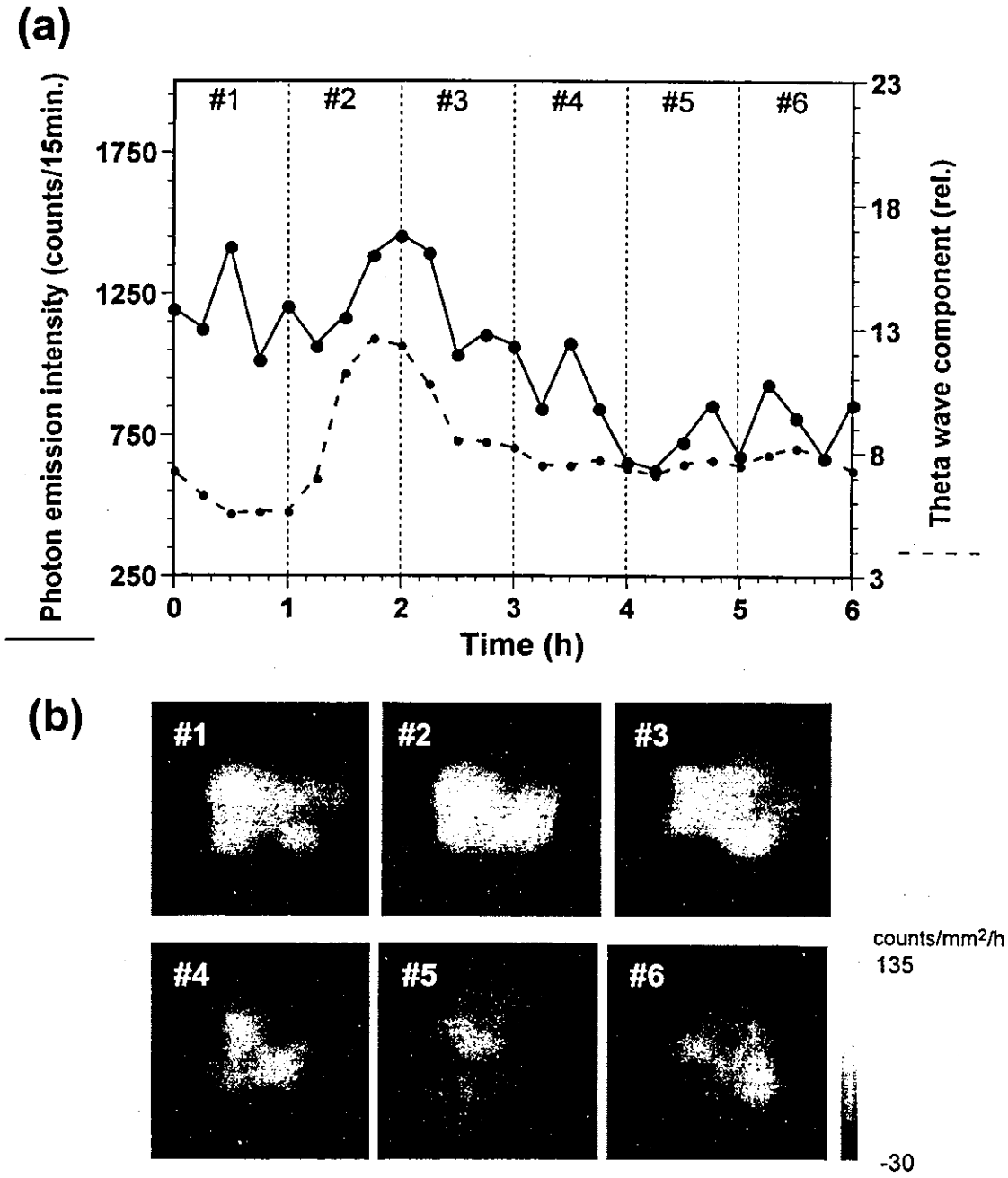

Fig. 7. (a) An example of temporal changes in biophoton emission intensity from a rat's brain and theta wave component of EEG power spectral density (ratio of component expressed in %, rel.). (b) Sequential images of photon emission for the time regions of #1-#6, indicated in (a).

anesthesia. One hemisphere of the brain was frontally-sectioned into slices of 500-μm thickness using a slicer. We obtained 10 sheets of slices, which were placed in a quartz chamber containing circulating artificial cerebrospinal fluid (ACSF) that was bubbled with a mixture of 95% oxygen and 5% CO_2. A reference

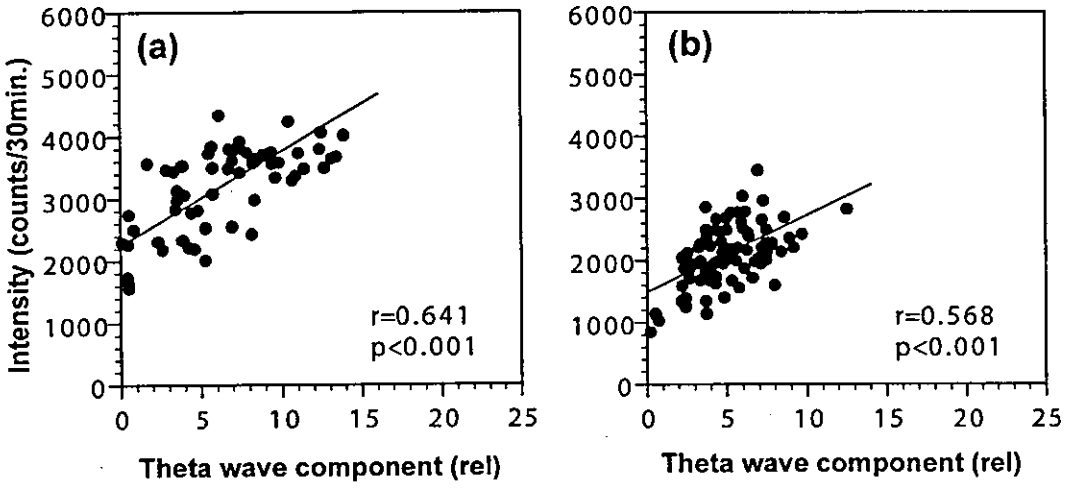

Fig. 8. Correlation analysis between biophoton emission intensity and theta wave component of EEG power spectra represented by 30-minute integration. (a) Correlation after having the bilateral bones removed and (b) without removing the bone. Correlation coefficients and statistical significance are indicated in the figures

spectrum observed under normal conditions is shown in Fig. 9 (a). This shows an emission spectrum ranging from 500 to 800 nm, with peaks around 530 nm and 610 nm and a shoulder at 670 nm. The dashed line in Fig. 9 (a) shows the spectral pattern measured under glucose deprivation in the ACSF. As can be seen in Fig. 9 (b), which shows temporal changes in the intensity before and after glucose deprivation, the photon emission intensity in the case of glucose deprivation was depressed by approximately 20% in comparison with normal (indicated by glucose (+)) conditions [7]. However, no significant differences in shape could be seen between the two spectral patterns, except for a minor depression of the intensity in the wavelength region between 600 nm and 700 nm. We also carried out analyses to compare the reference spectrum with spectra taken under conditions where glutamate or rotenone had been added for neuronal activation or for inhibition of the mitochondrial electron transfer chain, respectively. Although a temporary increase in the emission intensity was observed in both cases after the treatments (suggesting a relationship between the photon emission and activation of the energy metabolism through the electron leakage in the respiratory chain [7]), once again no remarkable changes were recognized in the spectral patterns in either case.

In order to investigate the emission mechanisms, we compared the spectral patterns of the slices with the chemiluminescence from unsaturated fatty acids, which were observed under gradual autooxidation with pure oxygen at 37°C. The three lines in Fig. 10 show the spectra of oxidized linoleic acid, linolenic acid and arachidonic acid, respectively. Linoleic acid exhibited temporal changes in its spectral pattern during autooxidation. The early stages of the autooxidation featured 3 peaks at around 530 nm, 630 nm and 700 nm, with spreading over 450-750 nm (data not shown). In the latter stages, enhancement of the emission intensity was observed, centered on the peak at 530 nm. In the case of linolenic acid, the spectral pattern ranged from 600-800 nm, with a dominant peak at 650 nm. Although a temporal increase in the photon-emission intensity during the autooxidation process was observed, no notable changes occurred in its spectral pattern. In the case of arachidonic acid, the chemiluminescence during the autooxidation showed a constant intensity in terms of photon emission. Its spectral pattern was also unchanged during the measurement period and the emission

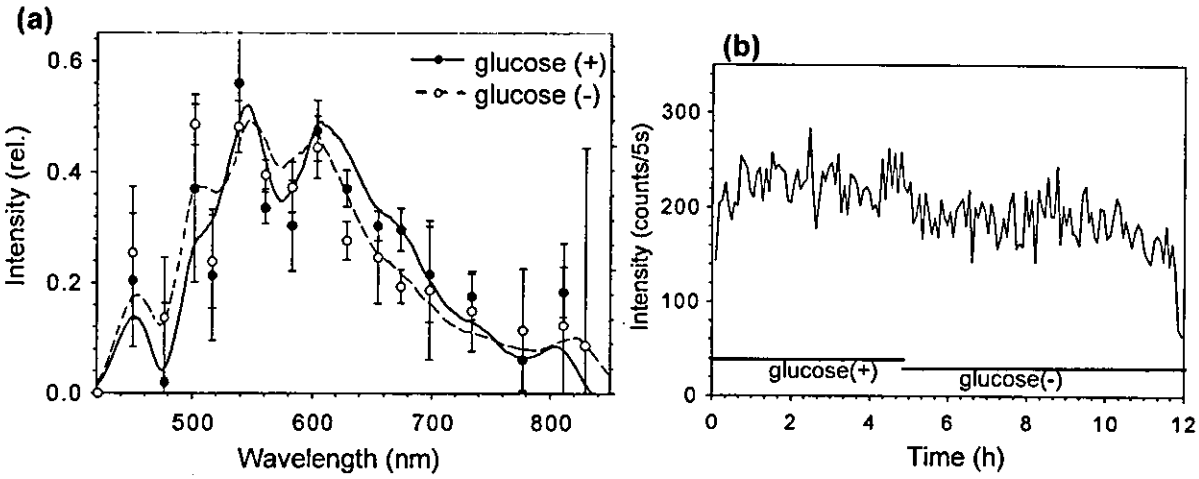

Fig. 9. (a) A biophoton emission spectrum of brain slices (solid line) in comparison with the conditions of glucose deprivation (dash line). (b) Temporal changes of the emission intensity of slices under the condition with glucose and without glucose in ACSF

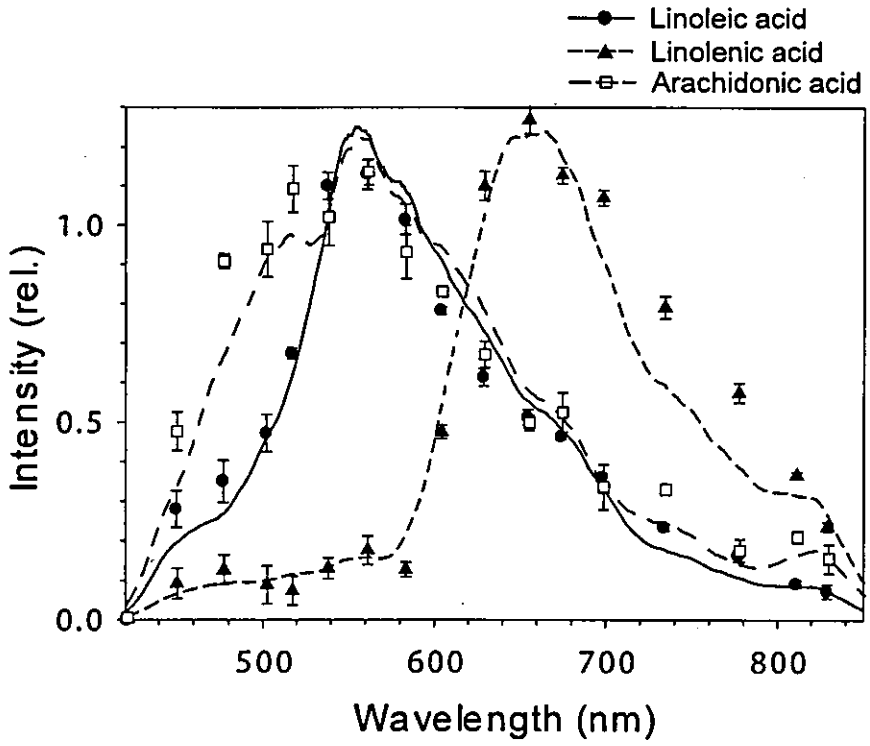

Fig. 10. Comparison of chemiluminescence spectra among linoleic acid (solid line with filled circle; later stage of oxidation), linolenic acid (dash line with filled triangle) and arachidonic acid (dash-dot line with open square) during autooxidation promoted with pure oxygen under 37°C.